Journal of The Electrochemical Society, 2020 **167** 124523

Catalyst-Integrated Gas Diffusion Electrodes for Polymer Electrolyte Membrane Water Electrolysis: Porous Titanium Sheets with Nanostructured TiO_2 Surfaces Decorated with Ir Electrocatalysts

Masahiro Yasutake,[1] Daiki Kawachino,[1] Zhiyun Noda,[1,2] Junko Matsuda,[2,3] Stephen M. Lyth,[3,4] Kohei Ito,[1,2,5] Akari Hayashi,[1,2,4,5,*] and Kazunari Sasaki[1,2,3,4,6,*,z]

[1]*Department of Hydrogen Energy Systems, Faculty of Engineering, Kyushu University, Fukuoka 819-0395, Japan*
[2]*International Research Center for Hydrogen Energy, Kyushu University, Fukuoka 819-0395, Japan*
[3]*International Institute for Carbon-Neutral Energy Research (WPI-I2CNER), Kyushu University, Fukuoka 819-0395, Japan*
[4]*Platform of Inter/Transdisciplinary Energy Research (Q-PIT), Kyushu University, Fukuoka 819-0395, Japan*
[5]*Next-Generation Fuel Cell Research Center (NEXT-FC) Kyushu University, Fukuoka 819-0395, Japan*
[6]*Center of Coevolutionary Research for Sustainable Communities, Kyushu University, Fukuoka 819-0395, Japan*

Novel catalyst-integrated gas diffusion electrodes (GDEs) for polymer electrolyte membrane water electrolysis (PEMWE) cells are presented, in which porous titanium microfiber sheets are etched in NaOH to generate a nanostructured TiO_2 surface, followed by arc plasma deposition (APD) of iridium nanoparticles. The porous titanium sheet acts as a gas diffusion layer (GDL); the nanostructured TiO_2 surface acts as a catalyst support with large surface area; and the iridium nanoparticles act as the electrocatalyst. The performance of these unique GDEs in PEMWE cells was optimized by etching in different NaOH concentrations to vary the nanostructure of the TiO_2; and by varying the Ir loading via the number of APD pulses. The current-voltage characteristics and the durability of the optimized GDEs were comparable to those reported in the literature using conventional Ir-based electrocatalysts, and electrolysis was achieved with current density up to 5 A cm^{-2}. The main advantages of this catalyst-integrated GDE include the very low iridium loading (i.e. around 0.1 mg cm^{-2}, or just one-tenth of the loading typically used in conventional PEMWEs); high electrolysis current density; the fabrication of stacks with fewer components; and the fabrications of thinner stacks. This could ultimately lead to smaller and lower cost PEMWE systems.
© 2020 The Author(s). Published on behalf of The Electrochemical Society by IOP Publishing Limited. This is an open access article distributed under the terms of the Creative Commons Attribution Non-Commercial No Derivatives 4.0 License (CC BY-NC-ND, http://creativecommons.org/licenses/by-nc-nd/4.0/), which permits non-commercial reuse, distribution, and reproduction in any medium, provided the original work is not changed in any way and is properly cited. For permission for commercial reuse, please email: permissions@ioppublishing.org. [DOI: 10.1149/1945-7111/abb37d]

Manuscript submitted May 21, 2020; revised manuscript received August 7, 2020. Published September 9, 2020. *This was paper 1758 presented at the Atlanta, Georgia, Meeting of the Society, October 13–17, 2019.*

Accelerating the introduction of renewable electricity is an essential step towards the replacement of fossil fuels, the suppression of CO_2 emissions, and the aversion of a climate crisis. To achieve the 2 °C scenario agreed at the COP21 meeting in Paris, by 2050, global energy-related CO_2 emissions must decrease considerably. This will require a dramatic increase in the share of renewable electricity.[1,2] Renewable energy resources such as solar and wind power are abundant, but their fluctuating nature is a major roadblock,[3–5] and renewable electricity supply depends on e.g. daily weather conditions. Therefore, energy storage is becoming increasingly important to act as a buffer for matching of renewable power generation with energy demand.[1,2]

Hydrogen is a sustainable chemical energy carrier for efficient energy conversion without the emission of carbon dioxide, and with the potential for long-term, large-scale energy storage. The widespread use of hydrogen will help to level out fluctuations in power generation and consumption.[6–9] In addition, hydrogen is attractive as a fuel for transportation, power generation, and as an industrial feedstock.[1,2] The Hydrogen Council recently presented their vision that hydrogen technologies will contribute to around a 20% reduction in global CO_2 emissions, and that hydrogen can cover approximately 18% of total final energy demand by 2050.[1] Electrolysis is becoming an increasingly important technology to supply a growing demand for hydrogen, enabling the production of CO_2-free hydrogen directly from renewable electricity.

Polymer electrolyte membrane water electrolysis (PEMWE) is one of the most attractive electrolysis technologies for high current density operation with high efficiency, and for production of high purity hydrogen to be used directly in e.g. fuel cell vehicles (FCVs).[10–12] Many research groups are therefore focusing on PEMWE research and development.[10,13–20] Lowering the operational and capital costs, improving the performance, and achieving sufficient durability are all requirements for widespread commercialization of PEMWEs. Power generation cost currently dominates the operating expense (OPEX) for hydrogen production using PEMWEs. However, over the past decade, the costs of solar and wind power have declined by over 60% and over 40%, respectively.[21,22] As the price of renewable electricity falls, the capital expense (CAPEX) will become predominant. This originates from the system cost, including e.g. the cost of the noble metal catalysts, the electrolyte, the gas diffusion layers, and the separators/bipolar plates.[21,22] In terms of the electrocatalyst cost, noble metals such as iridium (often in the form of iridium oxide), are used as electrocatalysts in PEMWE cells, with high loading in the anode (typically from 1 to 2 mg cm^{-2}). Therefore, high materials cost is an important technological issue. In addition, platinum is often used to improve electrical contact with the titanium-based gas diffusion layers (GDLs).[23] Considerable reduction of the use of noble platinum-group metals (PGMs) is therefore essential for widespread use of PEMWEs with reasonable CAPEX. In support of this, e.g. in 2019, the Hydrogen and Fuel Cell Strategy Council of the Japanese government set specific targets for PGM loading in PEMWE technologies of 2.7 mg W^{-1} by 2020, and 0.4 mg W^{-1} by 2030.[24]

There are various approaches for reducing PGM loading in PEMWEs, such as suitable control of novel Ir catalyst morphologies,[25,26] or Ir alloying with other metals.[27–30] Currently, unsupported Ir-based electrocatalysts are used as the industry standard, typically made of IrO_2 powders. However, the use of supported Ir-based catalyst nanoparticles has the potential to significantly improve the mass activity, creating structures analogous to Pt/C electrocatalysts in polymer electrolyte fuel cells (PEFCs). To date, several researchers have developed Ir-based electrocatalysts dispersed on thermochemically stable supports. High surface area carbons (e.g. carbon black) are widely used as catalyst supports for PEFCs, but these cannot be applied in PEMWE cells due to the high

*Electrochemical Society Member.
zE-mail: sasaki@mech.kyushu-u.ac.jp

potential (>1.5 V) and strongly acidic environment, which lead to severe carbon corrosion.

In contrast, metal oxides and carbides such as titanium oxide,[31–33] tin oxide,[34–37] tungsten oxide,[38] niobium oxide,[39] indium tin oxide,[40] tantalum carbide,[41] titanium carbide,[42] and silicon carbide[43] are relatively stable in such severe environments, and as such they could be applicable as PEMWE catalyst supports. Metal oxide supports have already been shown to have enhanced stability against fluctuations in potential and start-stop cycling in PEMWEs and PEFCs, and therefore their use could lead to improvements in cell durability.[44–49] However, the electrical conductivity of metal oxides is relatively low compared with metals or graphitic carbons. The grain boundary resistance in polycrystalline materials can further suppress cell performance.[34,35] Minimizing the overall electronic pathway through metal oxides is thus desirable if metal oxide supports are to be applied to PEMWE cells.[47–49]

In the case of titanium metal, the surface has a thin native oxide layer, which is thermochemically stable in PEMWE anodes. Furthermore, titanium oxide nanostructures with relatively large surface area can be created on the surface of titanium via etching in NaOH.[50–53] As such utilizing surface oxidation of titanium GDLs is a potentially interesting approach for the creation of novel electrodes for PEMWE cells. Novel gas diffusion electrodes for PEFCs and PEMWE cells have previously been developed, combining e.g. porous titanium[50–53] or carbon[52,54,55] catalyst supports, the GDL, and the current collector. In particular, preliminary studies using porous Ti sheets for PEMWEs focused on comparison with carbon-based sheets,[52] and the effect of donor doping of TiO_2 on porous Ti sheets.[53] However, systematical studies on the electrochemical characteristics, electrochemical durability, and subsequent micro-structural analyses are still needed to verify the applicability of such new types of electrodes.

Here, we present an alternative concept for PEMWE cells, namely "catalyst-integrated gas diffusion electrodes" (GDEs). As liquid water in addition to gaseous oxygen is transported within such PEMWE anode layers, these GDEs can also be denoted as "porous transport layers" or "mass diffusion electrode". Porous titanium microfiber sheets are etched in NaOH to generate a nanostructured titanium oxide surface, followed by arc plasma deposition (APD) of iridium nanoparticles. The porous titanium sheet acts as a gas diffusion layer (GDL) and an electron conducting pathway; the nanostructured titanium oxide surface acts as a catalyst support with large surface area; and the iridium nanoparticles act as the electro-catalyst, as schematically shown in Fig. 1. In general, both Ti-based and Ir-based materials are thermochemically stable under PEMWE conditions.[56] Despite the high resistivity of the titanium oxide layer, the electronic pathway through it is relatively short. The integrated nature of the GDEs is also expected to minimize interfacial resistances between different components. The main advantages of this catalyst-integrated GDE are expected to be a decrease in the PGM catalyst loading; simplification of the PEMWE cell structure and fabrication process; and a reduction in the number of separate cell components, ultimately lowering the manufacturing cost. Metal-based porous electrodes have already been applied in various electrochemical systems, such as dimensionally stable anodes for the chlorine-alkali industry,[57] polymer electrolyte fuel cells,[58] solid oxide fuel cells,[59] direct methanol fuel cells,[60] and regenerative polymer electrolyte fuel cells,[61] where such electrodes could be regarded as gas diffusion electrodes.

Experimental

Preparation of Catalyst-Integrated GDEs.—The procedure for preparing the electrodes is summarized in Fig. 2. Three different titanium sheets were used as substrates: (i) titanium microfiber sheets with nominal porosity of ca. 70% (Nikko Techno, Ltd., Japan); (ii) titanium microfiber sheets with nominal porosity of ca. 50% (Nikko Techno, Ltd., Japan); and iii) titanium sintered sheets with nominal porosity of ca. 40% (Toho Tech Co., Japan). Average porosity values of these three kinds of (eight) samples by measuring their thickness and weight were 75.1 ± 2%, 53.6 ± 3%, and 47.8 ± 2%, respectively. The inaccuracy may arise from e.g. the surface roughness of such porous materials, affecting their thickness as measured by micrometer. The titanium microfiber sheets have a thickness of ca. 200 μm and are made up of interconnecting titanium microfibers with individual cross sections of approximately 10 μm by 10 μm. The titanium sintered sheets have a thickness of ca. 40 μm and are made up of interconnecting titanium grains approximately 10 to 30 μm in diameter. Figure 3 shows representative scanning

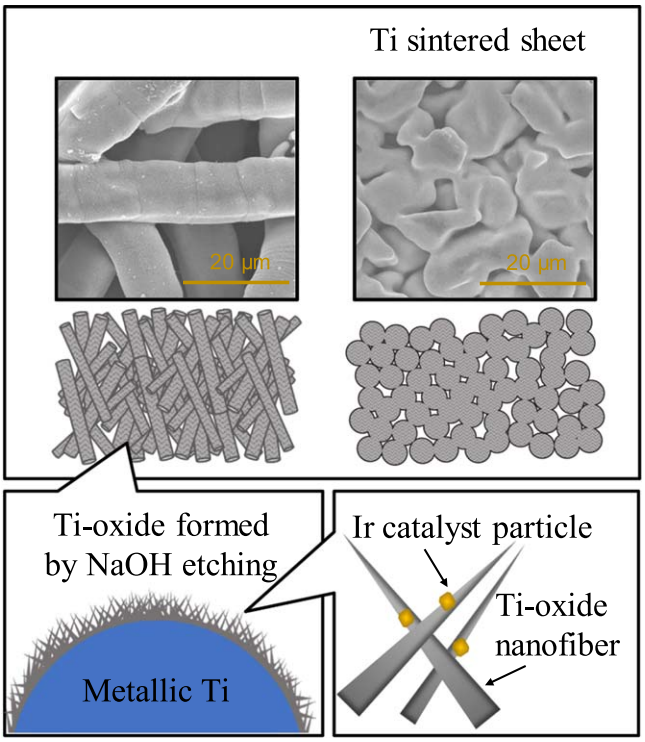

Figure 1. Schematic diagram showing the concept of the novel catalyst-integrated gas diffusion electrode (GDE) with a porous titanium sheet gas diffusion layer (GDL), nanostructured titanium oxide as an electrocatalyst support, and iridium-based nanoparticles as electrocatalysts.

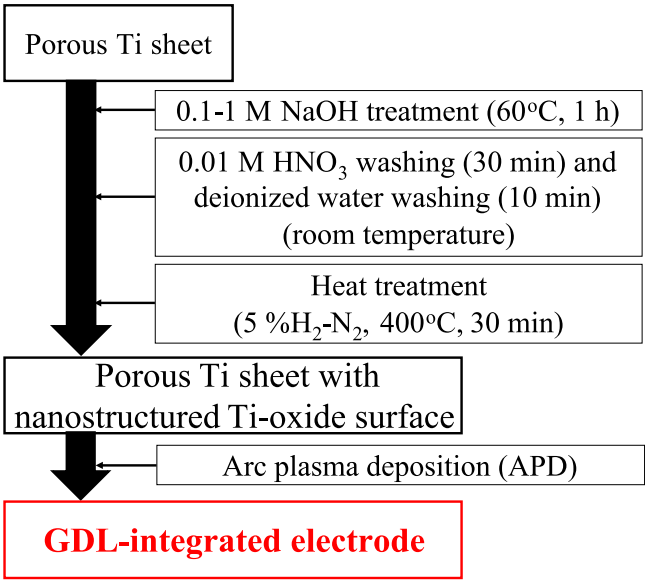

Figure 2. Preparation procedure of the novel catalyst-integrated GDEs.

electron microscopy (SEM) images of (a), (b) the surface, and (c), (d) cross-sections of: (a), (c) the titanium microfiber sheet (70% porosity), and (b), (d) the titanium sintered sheet (40% porosity). The cross-sectional images were taken after infiltration with epoxy resin (cold-setting epoxy resin, NER-814M, Nisshin EM Co., Ltd., Japan).

In order to increase the surface area of the titanium oxide surface layer, chemical etching with NaOH solution was performed. First, titanium sheets were etched in aqueous NaOH solution (Kishida Chemical Co., Ltd., Japan) at 60 °C for 1 h. The NaOH concentration was varied between 0.1 M and 1.0 M. Thereafter, the etched titanium sheets were washed under ultra-sonication in 0.01 M HNO_3 solution (Kishida Chemical Co., Ltd., Japan) for 30 min, and then washed in deionized water at room temperature for 10 min for complete neutralization. Heat treatment was then performed at 400 °C in 5% H_2-N_2 gas (50 ml min^{-1}) for 30 min, with a heating rate of 5 °C min^{-1}. The specific surface area of the titanium sheets was quantified by Brunauer–Emmett–Teller (BET) nitrogen adsorption measurements (BELSORP-mini II-VS, BEL Japan). Preliminary results reporting the optimization of major preparation conditions have been published elsewhere.[51–54]

Metallic iridium was deposited onto the NaOH-etched titanium sheets at room temperature, via arc plasma deposition (APD, Advanced RIKO, Inc., Japan),[62] using a vacuum pressure of 10^{-3} Pa; a discharge voltage of −100 V; a capacitance of 1080 μF; and a discharge frequency of 3 Hz. The iridium loading was controlled by varying the number of APD pulses.[52]

Characterization of Electrodes.—The microstructure of the fabricated Ir/TiO_2/Ti GDEs was observed by field emission scanning electron microscopy (FESEM, SU-9000, Hitachi High-Technologies Co., Japan), and scanning transmission electron microscopy (STEM, JEM-ARM200F, JEOL, Ltd., Japan) in combination with energy dispersive X-ray spectroscopy (STEM-EDS). The acceleration voltages of FESEM and STEM were 30 kV and 200 kV, respectively. Cross-sectional samples of electrodes were prepared by using focused-ion beam scanning electron microscopy (FIB-SEM, Versa 3D, FEI). The particle size of iridium catalysts was quantified from STEM images by using image analysis software (Scandium, Seika Co., Japan). The crystal structure of iridium-based nanoparticles was identified by analyzing fast Fourier transform (FFT) images in high-resolution STEM analysis.

The dependence of surface structures on the specific surface area of the titanium sheets after NaOH etching with different NaOH concentrations was evaluated using BET measurements. Ir loading was calculated by using a calibration curve prepared by measuring the Ir loading per unit area on carbon papers (instead of titanium sheets) by thermogravimetry (Thermo Plus TG8121, Rigaku Co., Japan) in air.[52] First, iridium was deposited onto the carbon papers via APD with different numbers of pulses, and the Ir loading per unit area and per pulse was obtained by measuring iridium mass after oxidative removal of carbon papers in the thermogravimetry equipment.

Preparation of MEAs.—The specifications of the PEMWE cells fabricated in this study are compiled in Table I. Membrane electrode assemblies (MEAs) were prepared with an electrode size of 1.0 cm^2, and a Pt loading of 0.5 $mg_{\text{-Pt}}$ cm^{-2} at the PEMWE cathode. To determine the effect of Ir loading on cell performance, the NaOH etching step used a fixed concentration of 1.0 M, and the Ir loading was varied from 0.043 to 0.086, 0.172, and 0.258 $mg_{\text{-Ir}}$ cm^{-2} at the PEMWE anode (1,000, 2,000, 4,000, and 6,000 pulses APD pulses, respectively). To evaluate the dependence of cell performance on NaOH etching concentration, the anode Ir loading was fixed at 0.086 $mg_{\text{-Ir}}$ cm^{-2} (2,000 APD pulses), and the NaOH concentration was varied between 0.1, 0.5, and 1.0 M.

The electrocatalyst paste for the PEMWE cathodes was prepared by dispersing standard Pt/C (Pt 46.5%, TEC10E50E, Tanaka Kikinzoku Kogyo Co., Japan), 99.5% ethanol, deionized water, and 5% Nafion solution (Sigma-Aldrich, 5 wt% Nafion in isopropanol), using an ultrasonic homogenizer. The Nafion ratio in the cathode electrocatalyst layer was set to be 28 wt%. This electrocatalyst paste was printed onto the electrolyte membrane

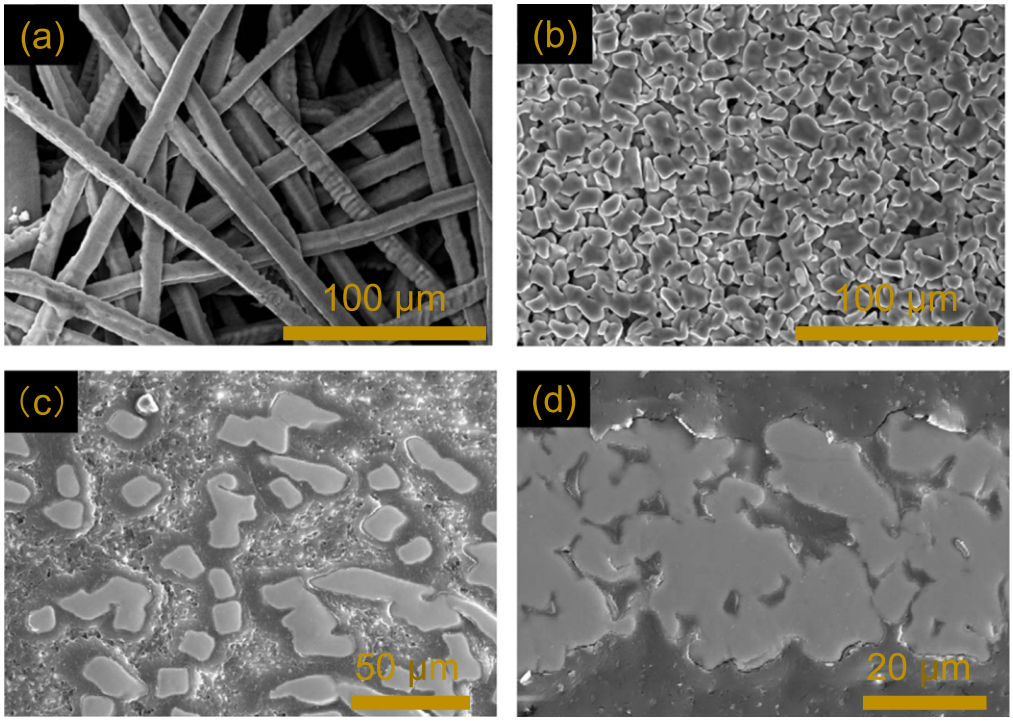

Figure 3. FESEM images of the porous titanium sheets, which act as the gas diffusion layer and current collector: (a), (b) surface images and (c), (d) cross-sectional images of (a), (c) titanium microfiber sheet (porosity 70%); and (b), (d) titanium sintered sheet (porosity 40%). The cross-sectional images (c), (d) were taken after infiltration with epoxy resin.

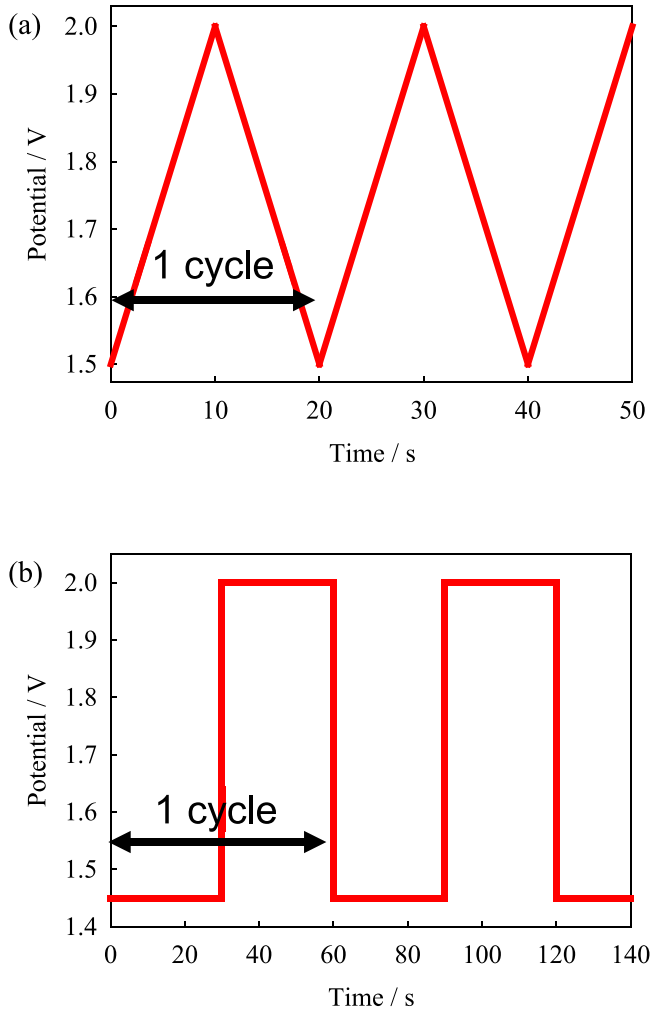

Figure 4. Schematic diagrams of durability test protocols: (a) Protocol (I);[66] and (b) Protocol (II).[64]

(Nafion117, E. I. du Pont de Nemours and Co.) using a spray printing system (C-3 J, Nordson Co.). Note that an MEA with a Nafion 115 electrolyte membrane was also prepared for comparison with data reported in the literature for commercial Ir-based catalysts.

The GDEs were applied as PEMWE anodes. The MEA was prepared by hot-pressing the anode with an electrolyte membrane, pre-coated with the Pt/C electrocatalyst layer on the cathode side, at 140 °C and 0.3 MPa for 180 s. Carbon paper (25BC, SGL Carbon) was used as the GDL on the cathode side. No additional GDL was needed for the anode. The tightening torque was typically set to be 4 Nm. MEAs with a smaller electrode size of 0.5 cm^2 (ca. 8 mm^{ϕ}) were prepared for measuring cell performance up to 5 A cm^{-2}. The dependence of the cell performance on hot-pressing pressure (3 MPa and 6 MPa), and tightening torque (from 2 to 12 Nm) in this cell setup was also evaluated.

Characterization of MEAs.—Current-voltage (I–V) characteristics of the PEMWE cells were evaluated at 80 °C using a commercial cell holder (Eiwa Co., Osaka, Japan). Teflon sheets with a thickness of 180 μm were used as gasket materials for gas sealing in the cell holder. Deionized water was supplied at 5 ml min^{-1}. Before the electrochemical measurements, deionized water was flowed for 2 h and the electrolysis cells were pre-treated by applying 5 triangular wave cycles between −0.5 V and 1.5 V at 600 mV s^{-1}. I–V curves were obtained by measuring current density with varying voltage applied from 1.3 V to 2.0 V at 50 mV s^{-1}, using an electrochemical analyzer (S11287, Solatron). Mass activity was determined as the current at 1.55 V per unit Ir mass,[63,64] and was used as a parameter for optimizing NaOH concentration, the number of APD pulses, and the Ti sheet structure.

An alternative current (AC) impedance analyzer (1255B, Solartron) was used to separate the ohmic resistance from the I–V characteristics. Activation overvoltage and concentration overvoltage were then separated following the procedure previously used for PEFC evaluation.[65] A Tafel plot was created with current density on the logarithmic x-axis, and the IR-free (ohmic-resistance-free) cell voltage on the y-axis. In the low current density region, 6 values were fitted with a linear regression.[65] The difference between the theoretical electromotive force (1.17 V at 80 °C, at ambient pressure) and the voltage of the linear regression line was taken as the activation overvoltage at the current density of interest. The deviation of IR-free voltage from the voltage in the linear regression line in the Tafel plot was taken as the concentration overvoltage. Concentration overvoltage was analyzed for optimizing the porous titanium sheet structure and for evaluating the cell performance at higher current densities. All electrochemical measurements were performed twice or more, and representative data was shown and further analyzed.

Electrochemical durability analysis.—The durability of the electrodes prepared by APD was evaluated using two different durability protocols, as described in Fig. 4. Protocol (I) consists of triangular wave potential cycles (2,000 cycles at 50 mV s^{-1}, between 1.5 V and 2.0 V), simulating fluctuations in renewable power generation proposed by Muto et al.[66] Protocol (II) consists of square wave potential cycles (2.0 V for 30 s and 1.45 V for 30 s, up to 10,000 cycles) proposed by Alia et al.[64] I–V curves and impedance were evaluated every 500 cycles.

Results and discussion

Formation of Nanostructured TiO_2 via NaOH etching.—The surfaces of the porous titanium sheets were observed by FESEM in order to clarify the effect of NaOH etching at different concentrations (0.1 M, 0.5 M, and 1 M) on the nanostructure, as shown in Fig. 5. After etching, the samples were washed in HNO_3 and heat treated at 400 °C. The as-received titanium fiber surface (Fig. 5a) is featureless and smooth. After etching with 0.1 M NaOH,

Table I. Specifications of the PEMWE cells fabricated in this study.

	Anode	Cathode
Gas Diffusion Layer	Porous Ti sheet after the surface treatment	Carbon paper
Electrode Area/cm^2	1	
Electrocatalyst	Ir-based electrocatalyst	46.5 wt.% Pt/C
Catalyst Loading/mg cm^{-2}	Ir: 0.043 per APD 1000 pulses	Pt: 0.5
Nafion Ratio/wt.%	(none)	28
Cell Temperature/°C	80	
Electrolyte Membrane	Nafion®115 (127 μm thickness), or Nafion®117 (183 μm thickness)	

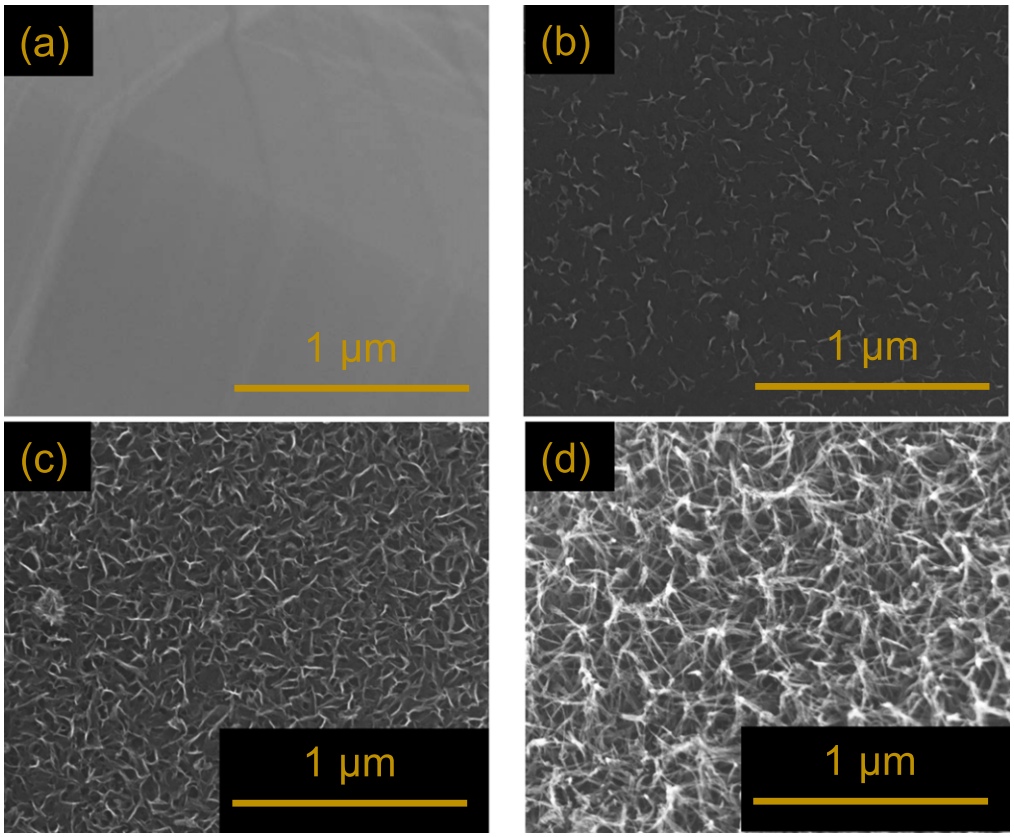

Figure 5. FESEM images of the surface of microfibers in titanium microfiber sheets: (a) without NaOH etching (as received); and with (b) 0.1 M; (c) 0.5 M; and (d) 1.0 M NaOH etching. Samples (b) to (d) were heat-treated at 400 °C in 5%H_2-N_2 for 30 min after NaOH etching.

nanostructures start to be formed on the surface (Fig. 5b). After etching at 0.5 M NaOH, this nanostructure becomes more pronounced (Fig. 5c), and the nanostructure is most developed after 1.0 M NaOH etching (Fig. 5d). The formed nanostructure is similar to the titanium oxide nanosheets and nanofibers after NaOH etching of titanium previously reported in the literature.[67–70] The microstructure is further investigated in the following sections.

The specific surface areas measured by BET were 1.0, 1.2, 1.4, and 1.7 $m^2\ g^{-1}$, respectively, showing a clear trend of increasing surface area with increased NaOH concentration, and confirming that the surface area can be controlled by NaOH etching. At first glance, a specific surface area of 1.7 $m^2\ g^{-1}$ may seem too low to be used as a catalyst support. However, it should be noted that this measurement includes the mass of the porous titanium sheet. The equivalent for PEFCs would be measuring the BET surface area of a carbon fiber based GDL coated with a Pt/C electrocatalyst. Since the surface area of such carbon fibers (geometrically $< 1\ m^2\ g^{-1}$ for ca. 10 μm^{ϕ} carbon fibers) is similar to that of the titanium fibers used in this study, the surface area of the whole electrodes would also be relatively low. It follows that the effective surface area of the nanostructured titanium oxide surface alone is much higher than this measured value, however it cannot be measured independently from the substrate. Given that complex nanostructure is clearly formed on the surface of the titanium microfibers, it is assumed that the specific surface area of this layer is sufficient to be useful as a catalyst support.

Figure 6a shows a cross-sectional STEM image of the titanium microfiber surface after 1.0 M NaOH etching and subsequent heat treatment at 400 °C. The presence of nanofibers with lengths of ca. 200 nm can be distinguished. Figures 6b and 6c show the corresponding EDS elemental intensity maps for titanium and oxygen, respectively. These images reveal that the nanofibers are titanium

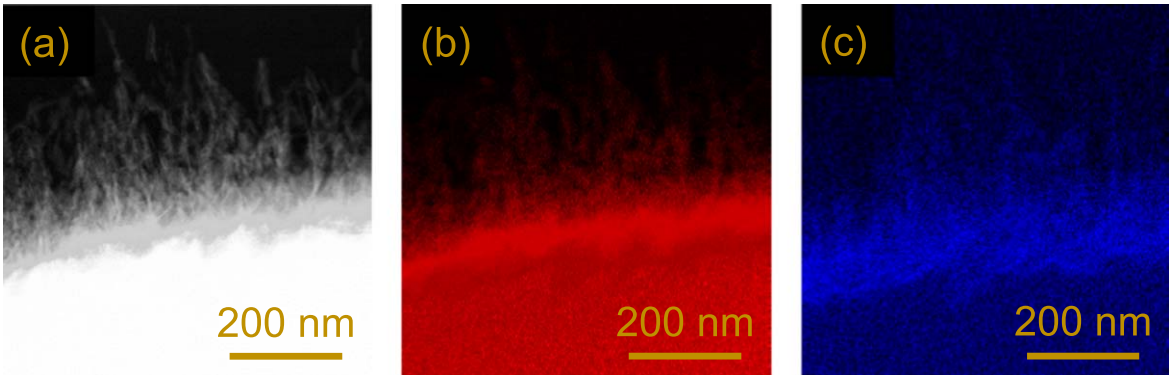

Figure 6. Cross-section of the nanostructured titanium oxide surface after 1.0 M NaOH etching and subsequent heat treatment at 400 °C: (a) STEM image; and the corresponding EDS elemental intensity maps for (b) titanium and (c) oxygen.

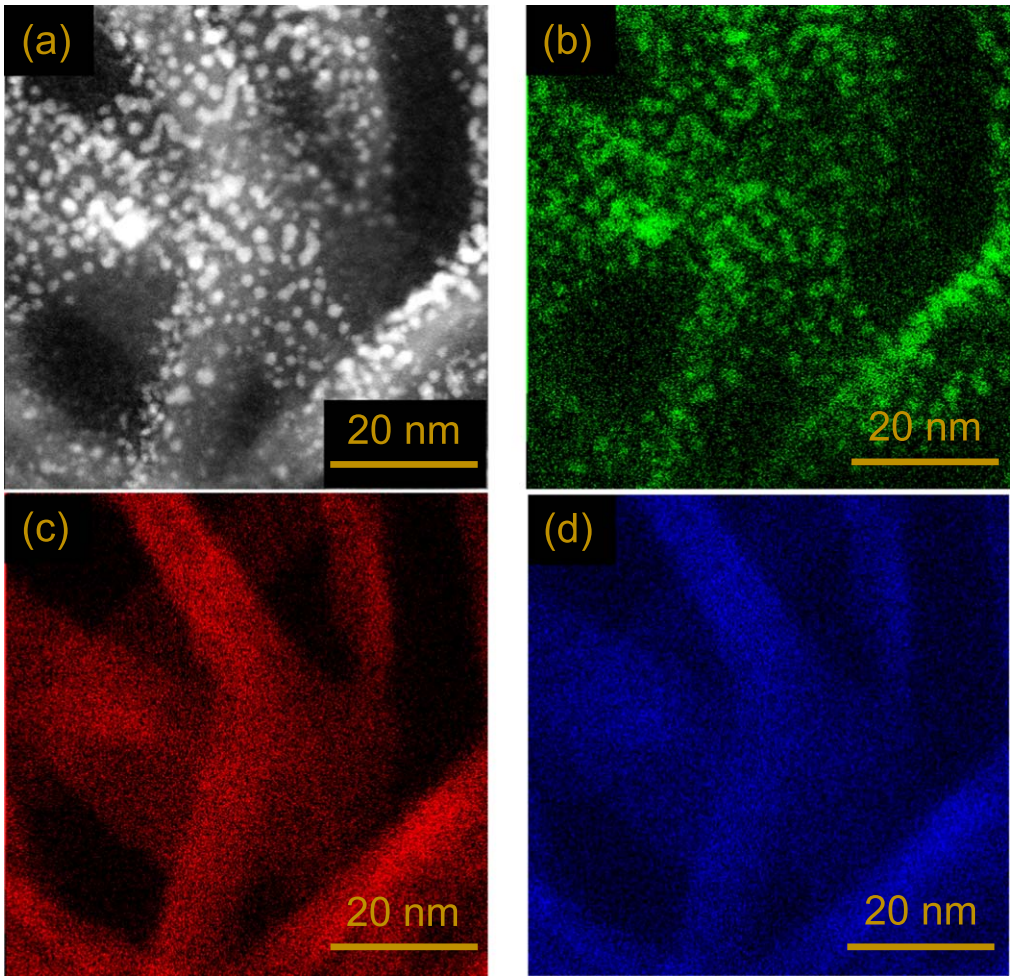

Figure 7. (a) STEM image of the catalyst-integrated GDE prepared using 2,000 APD pulses. Corresponding EDS elemental intensity maps for: (b) iridium, (c) titanium, and (d) oxygen.

oxide. This is in agreement with Kawachino et al.[70] who previously reported that titanium oxide nanofibers prepared using similar conditions had anatase structure (TiO_2). The growth mechanism is reported to involve the formation of nanosheets, which then curl to form nanotubes.[67–69]

***Deposition of iridium electrocatalysts* via *APD*.—**Iridium electrocatalyst deposition onto the nanostructured TiO_2 surface was achieved via APD. For every 1,000 pulses, the corresponding Ir loading was 0.043 $mg_{\text{-Ir}}$ cm^{-2}, confirmed by the thermogravimetric analysis. The effect of iridium loading on the microstructure of the electrocatalyst layers was investigated by using 2,000 or 4,000 APD pulses (i.e. 0.086 or 0.172 $mg_{\text{-Ir}}$ cm^{-2}). The NaOH etching concentration was fixed at 1.0 M. APD is a line-of-sight technique, and thus the resulting microstructure is different at the top surface or the sides of the microfibers, with most of the deposited Ir nanoparticles located at the top surface of the porous Ti sheets, causing a certain inhomogeneity in the Ir distribution.[70] All micrographs in this paper are from the top surface of the titanium sheets, where the local Ir loading is expected to be highest.

Figure 7a shows an STEM image of the titanium nanofiber surface after 2,000 APD pulses, whilst Figs. 7b–7d show the corresponding EDS elemental intensity maps for iridium, titanium, and oxygen, respectively. While it is difficult to determine the diameter of the titanium nanofibers from Fig. 6a, the STEM image in Fig. 7a confirms that the diameter of the nanotubes formed via NaOH etching is ca. 10 nm. The titanium and oxygen intensity maps overlap, confirming that the nanostructured material is indeed titanium oxide. Individual Ir nanoparticles are clearly observed as bright spots decorating the TiO_2 nanofibers, with an average diameter of 2.2 nm. Meanwhile, Fig. 8 shows the surface after 4,000 APD pulses. In this case, there is a high degree of connectivity between the iridium nanoparticles, forming an almost continuous iridium-based film due to the much higher loading.[50] But this leads to very weak EDS intensity for oxygen in Fig. 8d. At a larger number of APD pulses (e.g., 6,000 pulses), thicker iridium-based films are expected to be formed.

Figure 9a shows a representative high-resolution STEM image of an Ir nanoparticle decorated on a TiO_2 nanofiber deposited (4,000 APD pulses). The presence of lattice fringes indicates a high degree of crystallinity. As shown in Fig. 9b, a fast Fourier transform (FFT) of the area highlighted in Fig. 9a corresponds to the $(11\bar{1})$ and (200) planes of iridium metal with fcc structure, and a lattice constant of 0.3839 nm [PDF No. 00-006-0598]. Lattice angles between the $(11\bar{1})$ and (200) planes indicate that the particle is observed from the [011] direction (Fig. 9b). These results confirm that the as-deposited iridium nanoparticles are in the metallic phase.

***Electrochemical performance: effect of NaOH concentration*.—**PEMWE single cell measurements were performed for NaOH concentrations between 0.1 and 1.0 M NaOH (Ir loading fixed at 0.086 $mg_{\text{-Ir}}$ cm^{-2}). The potential cycling durability was evaluated using Protocol (I). Figure 10a shows the I–V characteristics before and after durability tests. Especially at low current density, the cell voltage decreases with increasing NaOH etching concentration, indicating that NaOH etching is indeed useful in

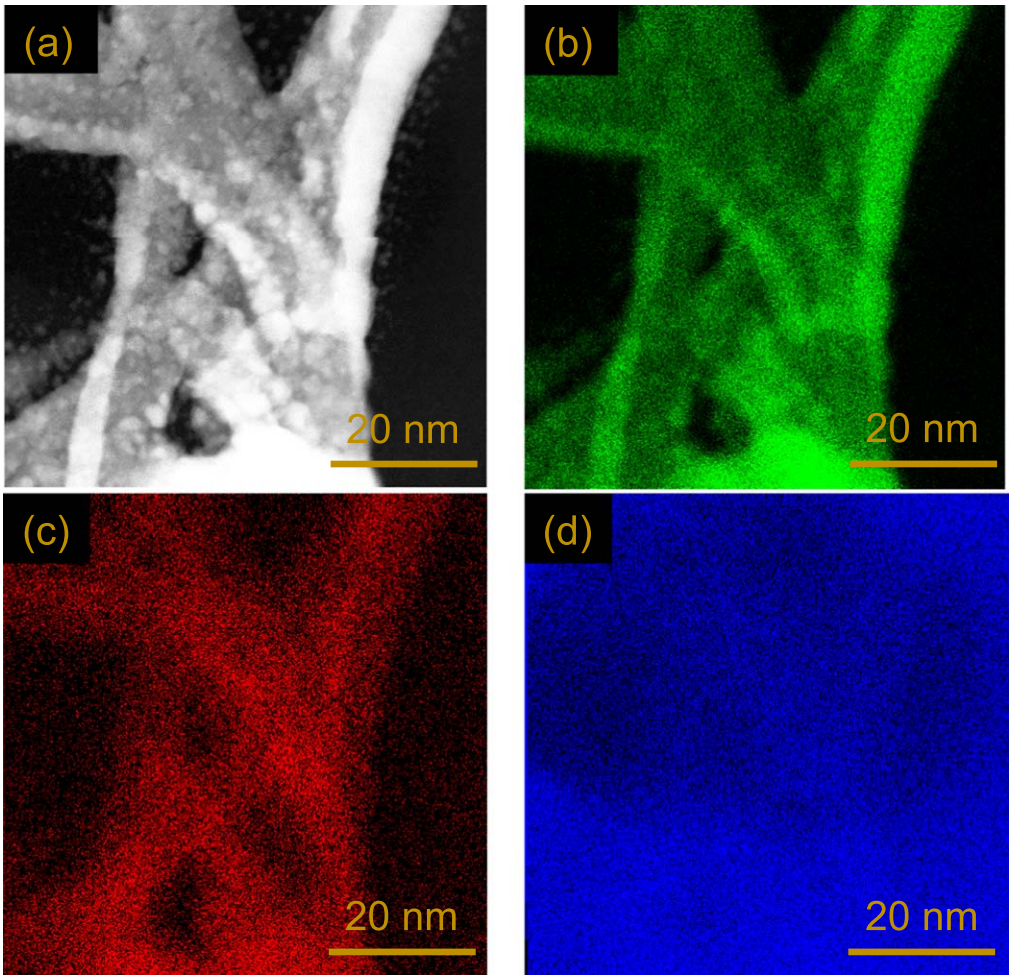

Figure 8. (a) STEM image of the catalyst-integrated GDE prepared using 4,000 APD pulses. Corresponding EDS elemental intensity maps for: (b) iridium, (c) titanium, and (d) oxygen.

terms of improving electrochemical performance. The performance after 0.1 M NaOH etching is similar to the case of no treatment. However, for 0.5 and 1.0 M NaOH etching, there is a significant improvement across the whole current density range. After potential cycling, the performance becomes worse in all cases, especially for lower concentration NaOH treatment. Meanwhile, the degradation is not as pronounced for the case of 1.0 M NaOH etching. This may be due to the higher surface area in this case, leading to better Ir distribution and improved interaction between these nanoparticles and the oxide surface, possibly preventing agglomeration and detachment. Figure 10b shows IR-free cell voltages for the cells after etching using 0.5 M and 1.0 M NaOH, before and after the potential cycling durability tests. This figure reveals that IR-corrected (i.e., IR-free) I–V characteristics for these cells are identical before the durability tests, indicating that the difference in cell performance arises mainly from the difference in ohmic resistance. After the potential cycling tests, however, electrochemical activity of the cell after 1.0 M NaOH etching is better than that after 0.5 M NaOH etching. Detailed microstructural analyses using higher magnification STEM (Fig. 11) show that the nanoparticles remain as metallic iridium, although the outermost surface of such catalyst nanoparticles could be partially oxidized.

Figure 11c shows the mass activity measured at 1.55 V for different NaOH etching concentrations. The mass activity (before potential cycling) increases with increasing NaOH concentration, which is attributed to improved dispersion of iridium electrocatalysts on the nanostructured surface as the NaOH concentration, and therefore the surface area increases. As such, 1.0 M NaOH etching was selected as the optimal condition for subsequent measurements.

The ohmic resistance (before potential cycling) also increases with increasing NaOH etching concentration (Fig. 10d). This is attributed to the progressive formation of the nanostructured titanium oxide layer, which is an electronic insulator. This increases the resistance to electron transport between the underlying titanium microfibers and the iridium electrocatalysts, as well as increasing the contact resistance between the titanium microfibers and the external cell components. As the effects of potential cycling on overvoltages could be complicated, further electrochemical studies combined with high-resolution microstructural analyses are made in a subsequent section.

Electrochemical performance: effect of Ir loading.—The electrochemical performance was also measured after varying the number of APD pulses between 1,000 and 6,000 (Ir loading from 0.043 to 0.258 $mg_{\text{-Ir}}\ cm^{-2}$). The NaOH etching concentration was fixed at 1.0 M. The potential cycling durability was evaluated using Protocol (I). Figure 12a shows the I–V characteristics before and after durability tests. Before potential cycling, the cell voltage decreases with increasing Ir loading (especially up to 4,000 APD pulses) across the whole current density range, indicating a clear improvement in performance as the Ir loading increases. After potential cycling, certain degradation in performance is observed for all of the electrodes. However, GDEs prepared using 4,000 and 6,000 APD pulses exhibit only a minor increase in cell voltage,

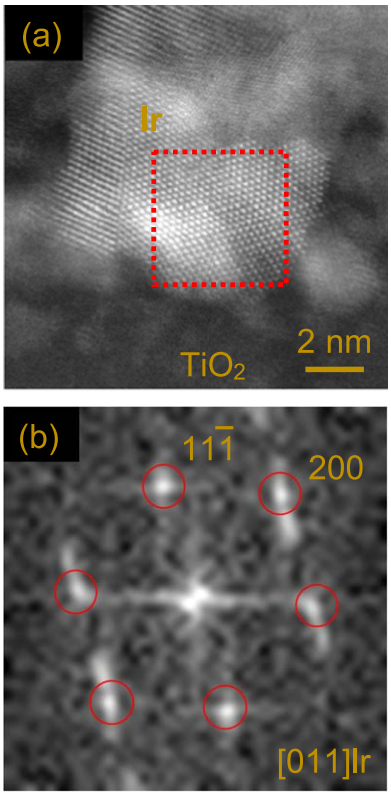

Figure 9. (a) Higher-magnification STEM image of iridium nanoparticles deposited onto the catalyst-integrated GDEs by APD (4,000 pulses, 0.172 mg_{-Ir} cm^{-2}). (b) Fast Fourier transform (FFT) of the region highlighted in red in (a). The FCC crystal structure corresponds to that of metallic iridium.

suggesting that higher loading leads to improved durability. Based on these results, the Ir loading for subsequent measurements was fixed at 4,000 APD pulses (i.e., 0.172 mg_{-Ir} cm^{-2}).

Figure 12b shows the change in mass activity with the number of APD pulses, before and after potential cycling. Before potential cycling, the mass activity steadily decreases as the loading increases. This is a consequence of increasing agglomeration and connectivity between the Ir particles as the loading increases, as observed in Figs. 7 and 8, decreasing the iridium utilization. Meanwhile, the retention of mass activity during potential cycling improves as the Ir loading increases, due to the increased stability of larger and more connected Ir nanoparticles.

Figure 12c shows the ohmic resistance of GDEs with increasing Ir loading. Before potential cycling, there is a slight decrease in ohmic resistance as the loading increases. Since the electronic resistance of the nanostructured titanium oxide layer is relatively high, this may indicate the formation of electronic conducting pathways through the deposited iridium layer as the loading increases, as seen in Figs. 7 and 8. After potential cycling, there is a small increase in ohmic resistance in all cases, possibly due to oxidation of the iridium nanoparticles. The ohmic resistances were 0.156 Ω and 0.168 Ω after 4,000 and 6,000 APD pulses, respectively. These values are similar to the membrane resistance of a fully-humidified Nafion 117 membrane (ca. 0.12 to 0.18 Ω[71,72]). This fact suggests that the ohmic resistances of the GDEs measured in this study are still relatively low. Conventional GDLs for PEMWEs are often coated with a layer of platinum in order to improve the electrical contact. We speculate that Ir or Pt contacts deposited with low loading via APD could help further decrease the PGM loading of the whole cell.

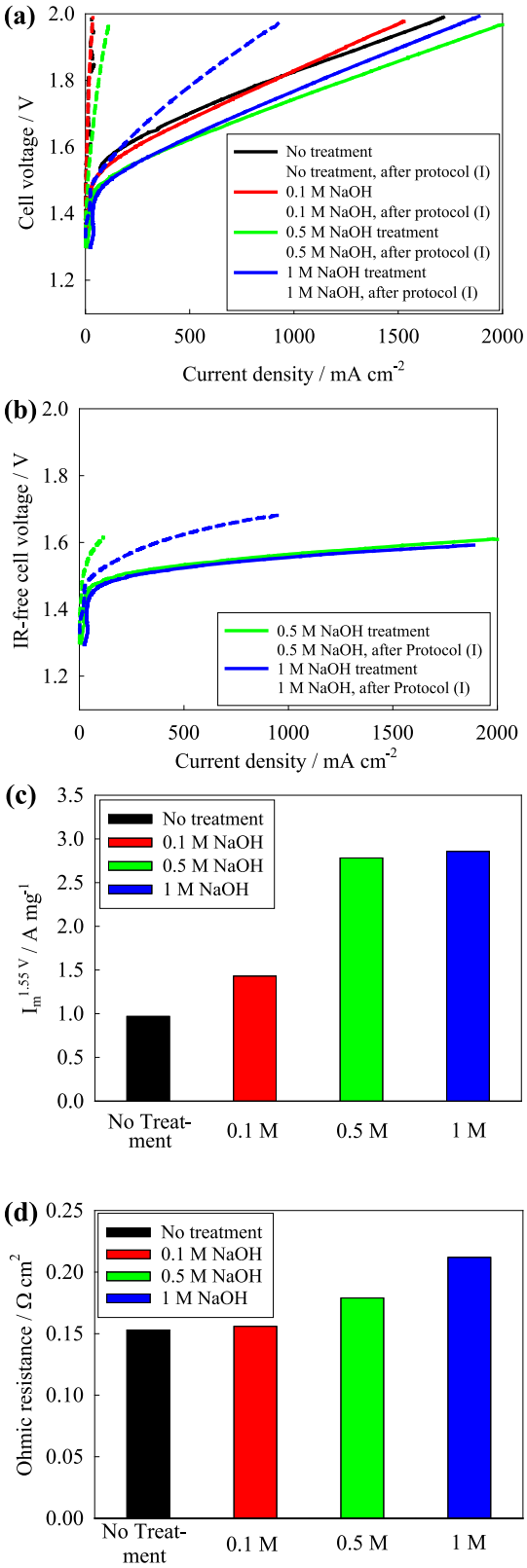

Figure 10. Electrochemical properties of PEMWE cells using catalyst-integrated GDEs prepared using 2,000 APD pulses and via NaOH etching with different concentrations. (a) I–V characteristics and (b) IR-free cell voltage before and after potential cycling using the Protocol (I); (c) initial mass activity, measured at 1.55 V; and (d) initial ohmic resistance.

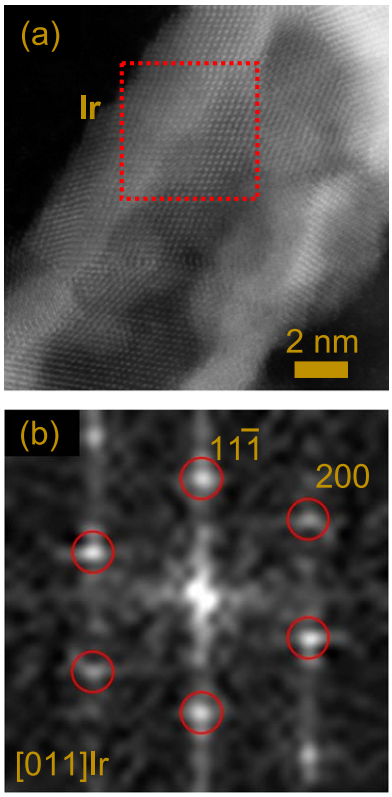

Figure 11. (a) Higher-magnification STEM image of iridium nanoparticles deposited onto the catalyst-integrated GDEs by APD (2,000 pulses, 0.086 $mg_{\text{-Ir}}$ cm^{-2}), after the I–V measurements (but before potential cycling). (b) Fast Fourier transform (FFT) of the region highlighted in red in (a). The FCC crystal structure corresponds to that of metallic iridium, even after the electrochemical measurements up to 2.0 V.

Electrochemical performance: effect of porous titanium sheet structure.—The microstructure and porosity of GDLs significantly affect the electrochemical performance (e.g. mass transport, conductivity etc).[73] Several researchers have previously studied the correlation between the cell performance and the GDL structure.[74,75] Therefore, the performance of PEMWE cells was evaluated for three different titanium sheets with different porosity and microstructure, as shown in Fig. 13: (i) a titanium sintered sheet with nominal porosity of 40%; (ii) a titanium microfiber sheet with nominal porosity of 50%; and (iii) a titanium microfiber sheet with nominal porosity of 70%. All GDEs were prepared using 1 M NaOH etching and 4,000 APD pulses. The I–V characteristics of all three cells are very similar, as shown in Fig. 13a. This indicates that changes in the nanoscale structure of the titanium oxide electrode surface, and the iridium electrocatalyst loading have a much greater impact on the PEMWE cell performance than the microstructure of the titanium supports. As such this technique can be generalized to different porous titanium substrates. The titanium microfiber sheet with 70% porosity exhibits the highest I–V performance. This is due to improved mass activity (Fig. 13b), possibly due to the larger available surface for NaOH etching in this higher porosity sample, and low concentration overvoltage (Fig. 13c) directly due to the higher porosity.

To gain further insight into the structure of the three different GDEs, they were infiltrated with resin, and cross sections were observed by FIB-SEM. Figure 14 shows cross-sectional SEM images and EDS iridium intensity maps of: (a), (b) the titanium sintered sheet with 40% porosity; (c), (d) the titanium microfiber sheet with 50% porosity; and (e), (f) the titanium microfiber sheet with 70% porosity. The top surface for APD deposition is facing the left hand side. Regions of high iridium distribution are highlighted with white lines added on the EDS maps, and the total lengths within these images are 111.4 μm, 126.7 μm, and 139.9 μm, for the titanium sheets with 40%, 50%, and 70% porosity, respectively. This indicates improved dispersion of the electrocatalysts and an increase in the triple-phase boundary for higher porosity GDEs, as reflected in the mass activity data.

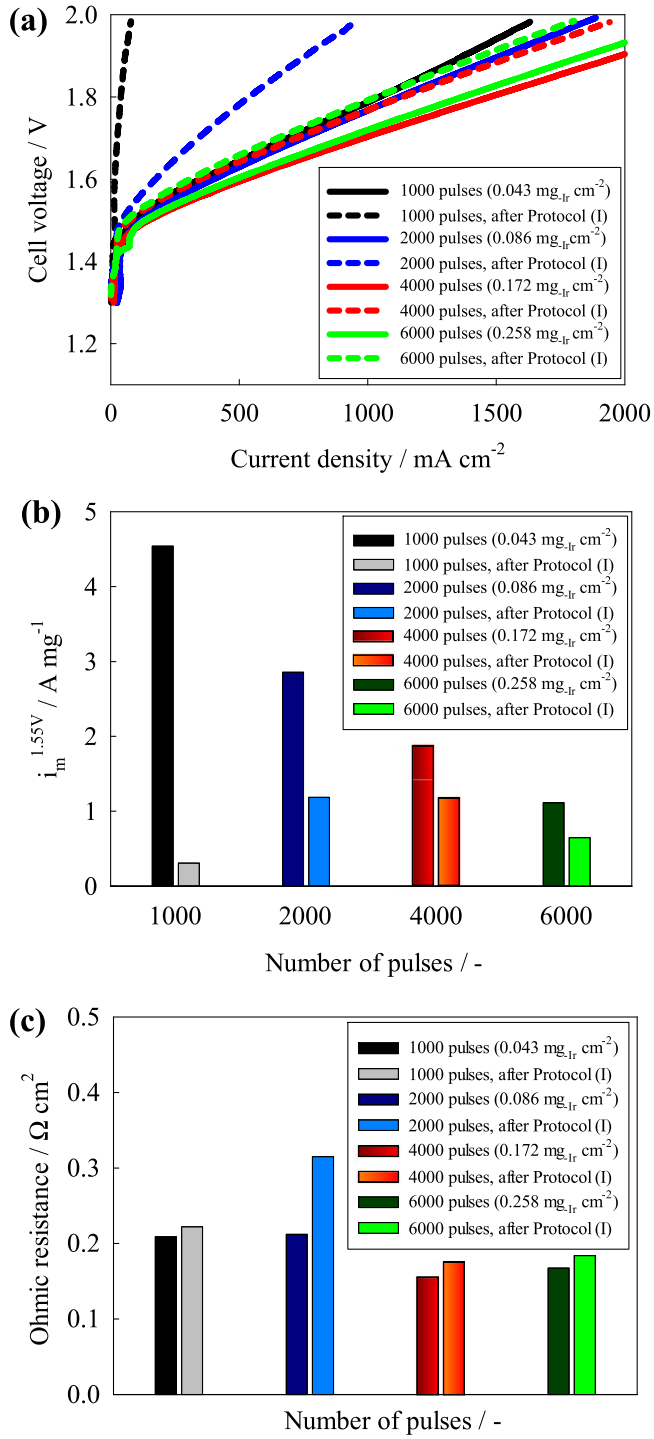

Figure 12. Electrochemical properties of PEMWE cells using catalyst-integrated GDEs prepared by varying the number of APD pulses. (a) I–V characteristics before and after potential cycling using the Protocol (I); (b) mass activity, measured at 1.55 V; and (c) ohmic resistance.

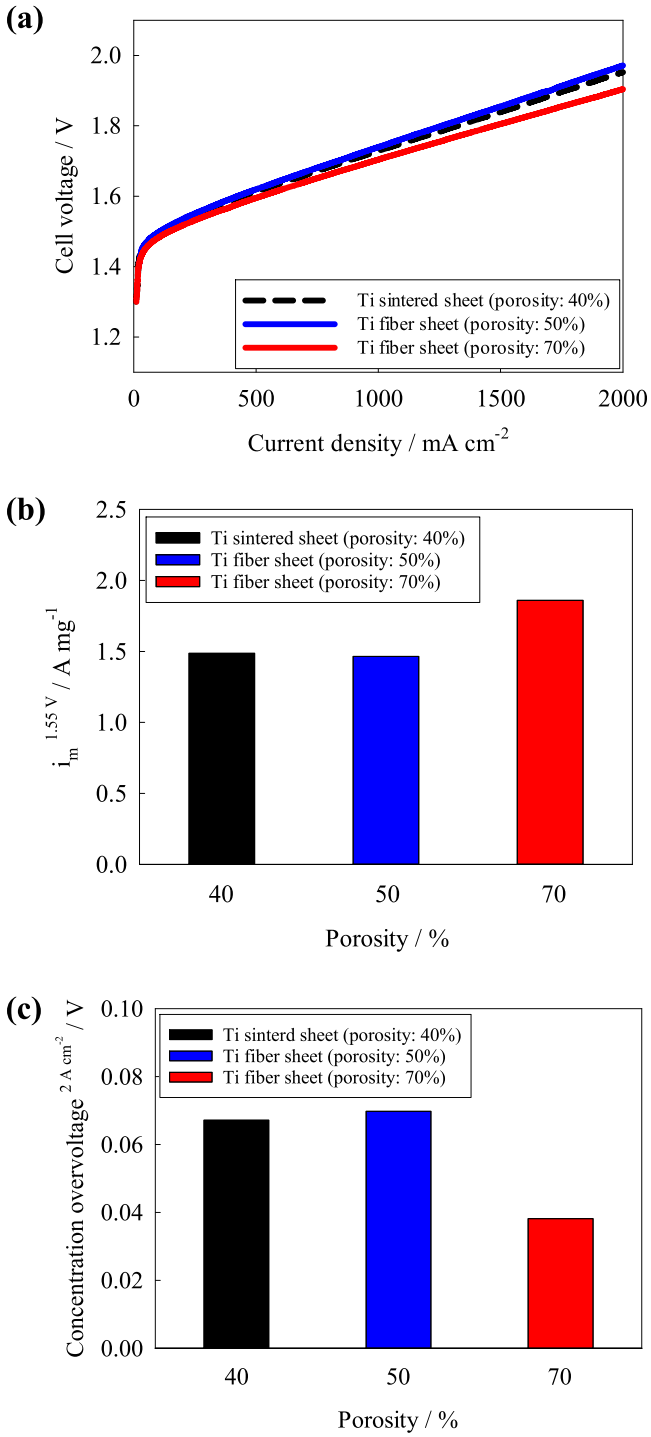

Figure 13. Electrochemical properties of PEMWE cells using catalyst-integrated GDEs prepared using porous titanium sheets with different microstructure and porosity. (a) I–V characteristics; (b) mass activity, measured at 1.55 V; and (c) initial concentration overvoltage measured at 2 A cm^{-2}.

Comparison with commercial Ir-based catalysts in the literature.—The best data obtained for the novel catalyst-integrated GDEs (titanium microfiber sheet with 70% porosity, 1.0 M NaOH etching, 4,000 APD pulses) was compared with conventional PEMWE cells from the literature. The data is shown in Fig. 15, in which the I–V characteristics are described along with the average values and the standard deviations, indicating the reproducibility of these measurements. Two different comparisons were made: one for cells using Nafion 115 (Fig. 15a); and another for cells using Nafion 117 (Fig. 15b). The reference electrocatalysts were $Ir/W_xTi_{1-x}O_2$ (Giner Inc.)[76] and Ir oxide (Surepure® Chemetals Inc.)[77] both of which used Nafion 115, and also Ir oxide (Alfa Aesar)[64] and Ir black (Johnson Matthey plc, UK),[64] both of which used Nafion 117. The Ir loading for each cell is also shown. All the cited literature data presents the I–V characteristics without correction for ohmic (IR) losses. For direct comparison with the literature data, cells using Nafion 115 and Nafion 117 were prepared, and the cell voltages without IR-correction are shown in Fig. 15. Overall, the cell performance of the GDEs is comparable to the previously published data using commercial catalysts in conventional PEMWE cells. In the case with Nafion 115, the catalyst-integrated GDE has better performance than both Ir-oxide based electrocatalysts (despite having lower, or similar

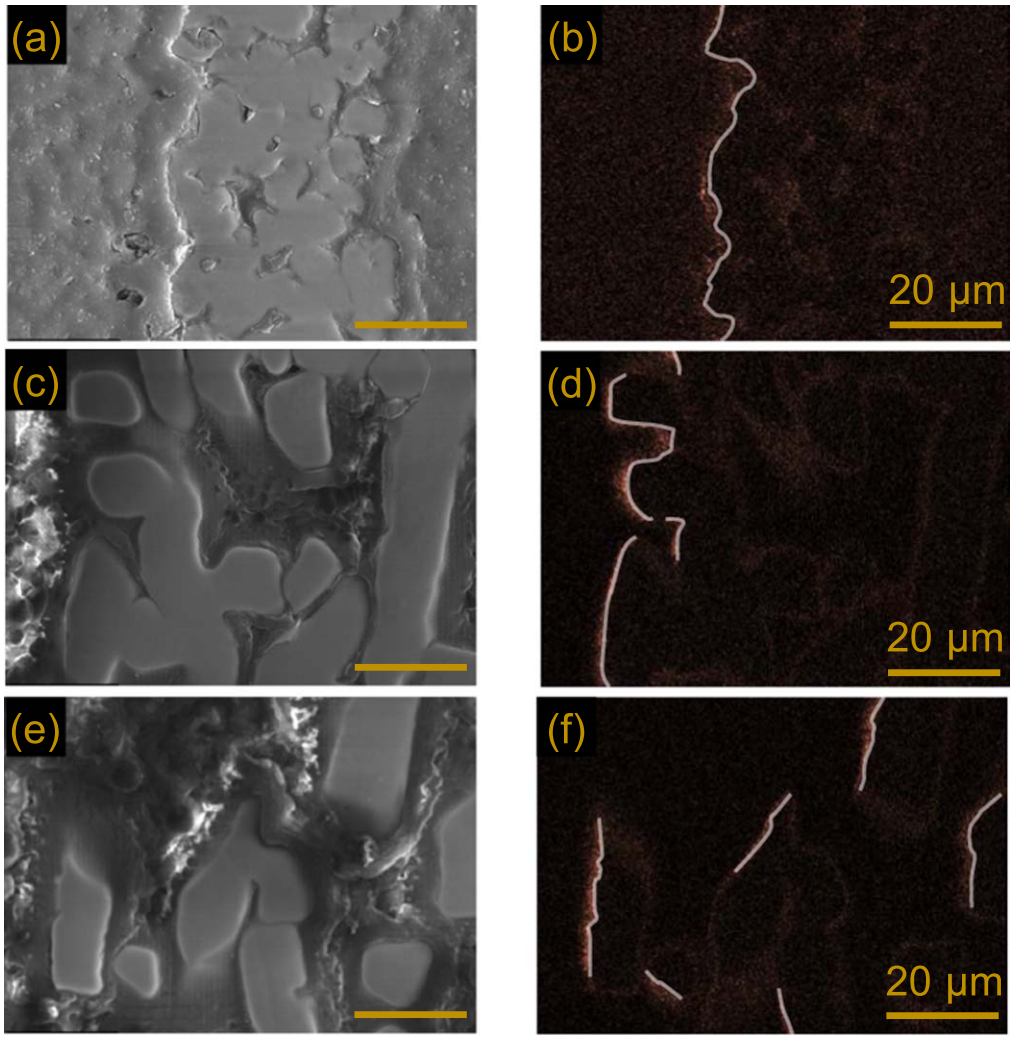

Figure 14. Cross-sectional FIB-SEM images (left) and the corresponding EDS elemental intensity maps for iridium (right): (a, b) titanium sintered sheet (porosity 40%); (c, d) titanium microfiber sheet (porosity 50%); and (e, f) titanium microfiber sheet (porosity 70%). APD was performed from the left side of the images, and white lines are used to highlight regions of iridium deposition in the EDS maps.

Ir loading in this study). The GDE has slightly lower performance compared with Ir/$W_xTi_{1-x}O_2$, although this may be explained by lower Ir loading. For Nafion 117, the electrochemical performance with the GDE is comparable to that with Ir oxide and Ir black in the low current density region, but slightly lower in the high current density region, despite similar Ir loading.

Comparison with commercial Ir-based catalysts after potential cycling.—The durability of the catalyst-integrated GDEs compared with conventional PEMWE cells fabricated using commercially available catalysts was investigated. The durability of the best-performing GDE (i.e. titanium microfiber sheet with 70% porosity, 1.0 M NaOH etching, 4,000 APD pulses), was compared with the literature data of conventionally prepared PEMWE cells using Ir oxide (Alfa Aesar, USA) and Ir black (Johnson Matthey, UK) catalysts.[64] The Ir loading for the commercial catalysts was 0.1 $mg_{\text{-Ir}}$ cm^{-2}, and Nafion 117 electrolyte membranes were used in all cases. The durability was evaluated using Protocol (II), which has been previously used for PEMWE evaluation in the literature.[64]

Figure 16 shows the I–V characteristics for each electrode before potential cycling, after 4,500 potential cycles, and after 9,000 potential cycles. Before potential cycling, in the low current density region, the cell performance of the catalyst-integrated GDE is comparable to the electrodes using commercial Ir-based catalysts reported in the literature, indicating that the catalytic activity is similar. However, in the high current density region, the cell voltage with the GDE was slightly higher. This is likely due to higher ohmic resistance, which generally dominates the overpotential in the high current density region. Such difference in ohmic resistance could be caused by differences in preparation and pre-treatment conditions of e.g. electrolyte membranes in various studies (i.e. H_2SO_4 treatment[72,78]). In addition, the ohmic resistance of the catalyst-integrated GDE could be higher due to the relatively insulating nanostructured titanium oxide layer. After 4,500 potential cycles, Ir oxide showed almost no degradation, whilst Ir black showed some minor degradation.[64] After 9,000 potential cycles, Ir oxide still only showed minor performance degradation, whilst the cell voltage of Ir black increased noticeably.[64] These results suggest that Ir-oxide has higher stability than Ir metal.[64] Meanwhile, the performance of the GDE decreased even after 4,500 cycles, but the overall increase in cell voltage is only around twice that of Ir black.

As shown in Fig. 17, the change in mass activity (Fig. 17a) and the ohmic resistance (Fig. 17b) of the catalyst-integrated GDEs during potential cycling was recorded every 1,000 cycles. The greatest decrease in mass activity is in the first 1,000 cycles, after which the rate of degradation is much slower. Similarly, the ohmic resistance increases rapidly in the first 1,000 cycles, after which it increases at a slower rate.

To gain insight into the degradation mechanisms behind the loss of mass activity and the increase in ohmic resistance during potential

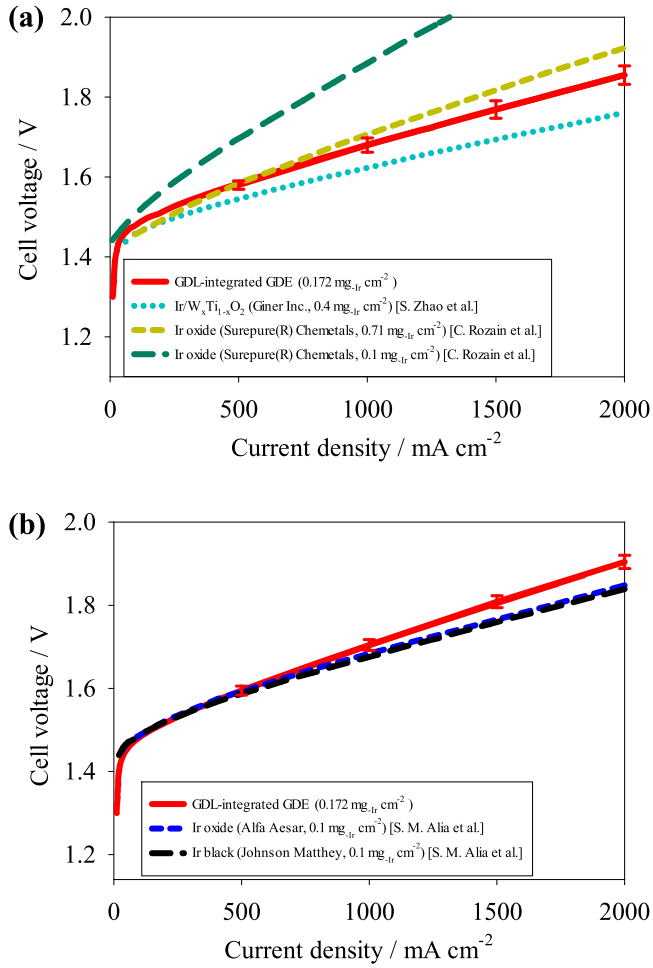

Figure 15. Electrochemical properties of PEMWE cells using catalyst-integrated GDEs compared with reference data from the literature: $Ir/W_xTi_{1-x}O_2$,[71] and Ir oxide.[59,72] The data is presented separately for different membrane thickness: (a) Nafion®115 (127 μm) and Nafion®117 (183 μm).

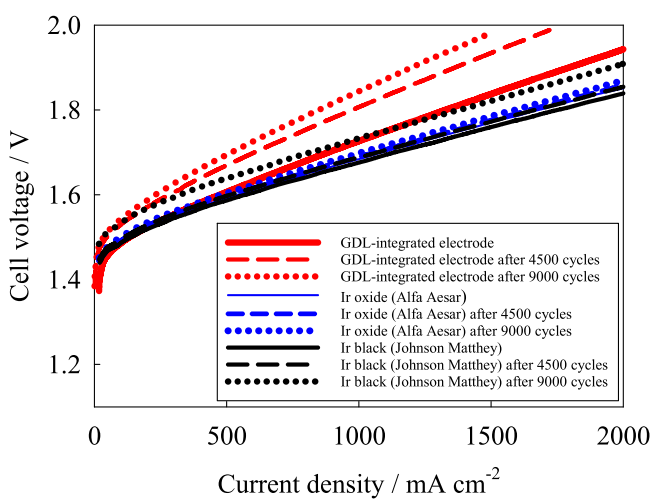

Figure 16. I–V characteristics of PEMWE cells using catalyst-integrated GDEs compared with conventional cells fabricated with commercial catalysts, before and after potential cycling using the durability Protocol (II).

cycling, microstructural characterization was carried out after potential cycling, as shown in Fig. 18. These STEM images show the presence of newly-formed iridium nanoparticles with much

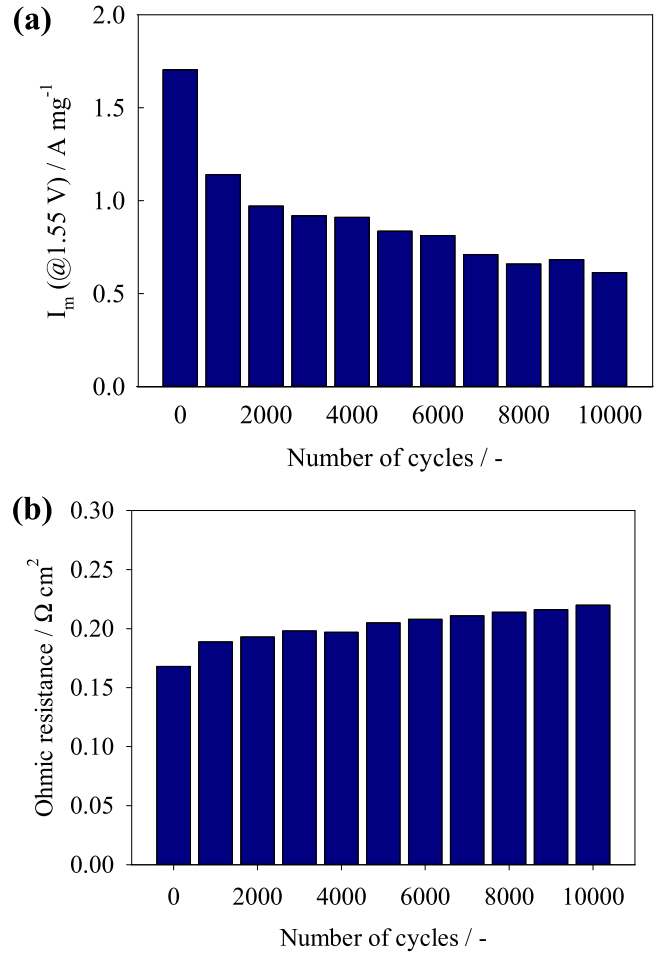

Figure 17. Variation of (a) mass activity measured at 1.55 V, and (b) ohmic resistance for a catalyst-integrated GDE over 10,000 potential cycles, following the durability Protocol (II).

larger diameter (~20 nm) than those originally formed by APD (~2 nm). Iridium dissolution is reported to occur above 1.8 V under PEMWE conditions.[79,80] Therefore, potential cycling between 1.45 and 2.00 V in Protocol (II) is expected to lead to repeated dissolution and reprecipitation of iridium, leading to nanoparticle growth via Ostwald ripening. In addition, the overlapping EDS elemental intensity maps for iridium and oxygen (Figs. 18b and 18d) indicate that iridium is partially oxidized during potential cycling. The EDS intensity maps for titanium (Fig. 18c) and oxygen (Fig. 18d) also hint at changes in the nanostructured titanium oxide support. Before potential cycling, the atomic ratio of titanium to iridium was 0.21, but this falls to 0.11 after potential cycling, suggesting a partial loss of titanium relative to iridium. This quantitative analysis suggests that the TiO_2 nanofibers can gradually dissolve during the severe durability tests up to 2.0 V.

The oxidization of iridium during potential cycling was confirmed by high-resolution electron microscopy. Figure 19a shows a high-angle annular dark-field STEM (HAADF-STEM) image of the Ir-based catalyst nanoparticles after potential cycling. The catalyst nanoparticles remain on the electrode, with a crystallite size of 2 to 3 nm. The lattice spacing estimated from the FFT image (Fig. 19b) of the highlighted region in Fig. 19a corresponds to the (111) planes of metallic iridium. Meanwhile, the selected-area electron diffraction (SAED) pattern in Fig. 19c taken from a 200 nm diameter region of the Ir-based electrocatalyst layer in Fig. 18a shows the diffraction pattern of metallic iridium overlapping with that of IrO_2. These results indicate that iridium metal coexists with IrO_2 in the electrocatalyst layer after potential cycling, possibly forming a

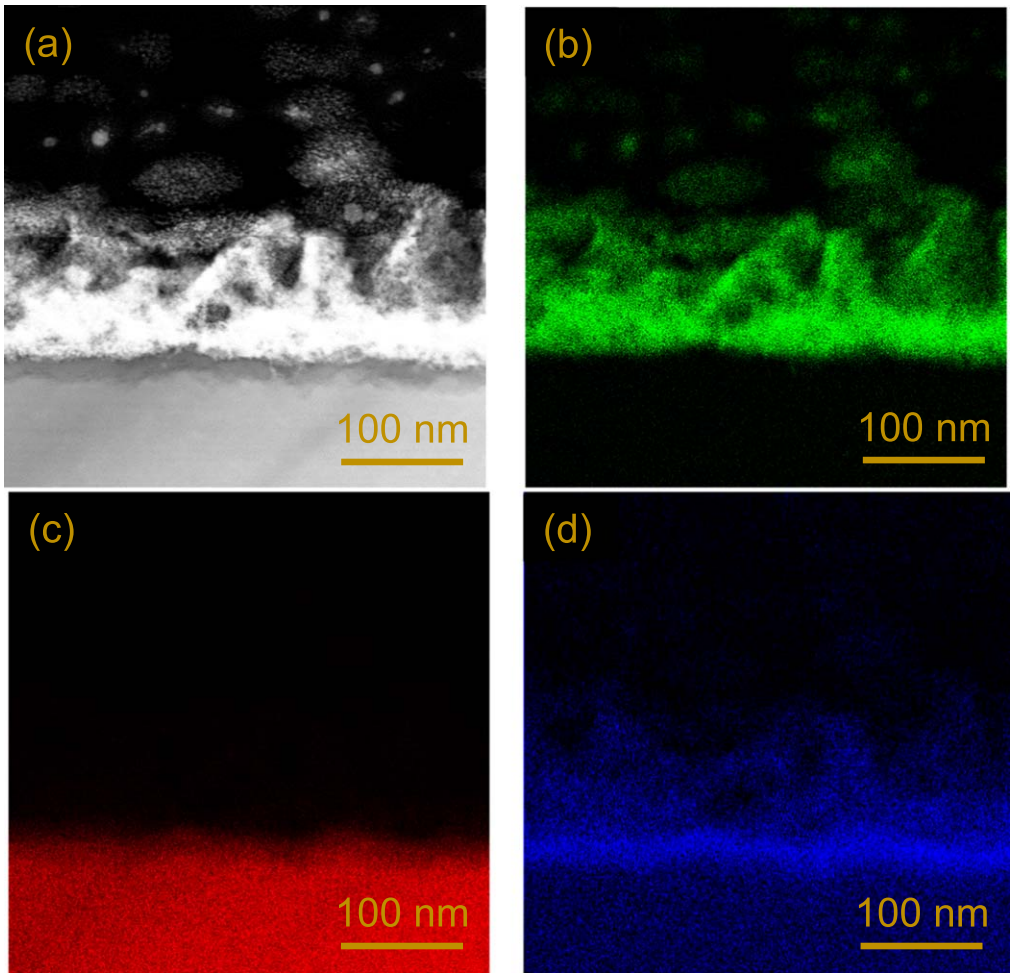

Figure 18. (a) STEM image of a catalyst-integrated GDE prepared using 1.0 M NaOH etching and 4,000 APD pulses, after 10,000 potential cycles using the durability Protocol (II). Corresponding EDS elemental intensity maps for: (b) iridium, (c) titanium, and (d) oxygen.

core–shell type structure where the outermost surface of metallic iridium core is oxidized to form IrO_2 shell.

As such, the decrease in mass activity for the catalyst-integrated GDEs during potential cycling can be attributed to a decrease in iridium utilization due to Ostwald ripening, iridium oxidization, and dissolution of the titanium oxide support, leading to detachment. The increase in ohmic resistance during potential cycling can be attributed to partial oxidation of the metallic iridium electrocatalyst, disrupting the electron conducing pathways. These results also suggest that further optimization of the PEMWE cells using these catalyst-integrated GDEs is needed, as well as more detailed characterization of the distribution of IrO_2 and Ir metal in the electrocatalyst layer. These points will be dealt with in a future study.

High current density operation.—Operation at high current density is an attractive advantage of PEMWE compared with alkaline water electrolysis and solid oxide steam electrolysis, and will contribute to the development of more compact systems. However, at high current density, the concentration overvoltage generally dominates PEMWE cell performance. In this section, the electrochemical performance of catalyst-integrated GDEs in PEMWE cells is evaluated at high current density, and the fabrication parameters (i.e. the tightening torque and the hot-pressing pressure) are optimized. MEAs with an electrode size of 0.5 cm^2 were evaluated up to 5 A cm^{-2}. Other conditions remained the same (i.e. titanium microfiber sheet with 70% porosity, 1.0 M NaOH etching, and 4,000 APD pulses).

Figure 20 shows the concentration overvoltage evaluated at 3 A cm^{-2}, using different cell tightening torques. The hot-pressing pressure was fixed at 3 MPa. The concentration overvoltage decreases significantly as the tightening torque increases. This is contrary to the trend typically observed in the literature,[81–84] and may be unique to the GDE structures developed in this study. Here, higher tightening torque is postulated to decrease the thickness of the GDEs without compromising the porosity too much, thus leading to improved mass transport. Higher tightening torque may also lead to better electrical contact between the titanium microfibers, decreasing the ohmic resistance. The hot-pressing pressure was also found to have an impact on the cell performance. The concentration overvoltage at 3 A cm^{-2} decreased from 0.109 V to 0.0521 V when the pressure was increased from 3 to 6 MPa.

Figure 21 shows the I–V characteristics and overvoltages, at 80 °C, of an optimized catalyst-integrated GDE with the iridium loading of 0.172 $mg_{\text{-Ir}}$ cm^{-2} at the anode in a PEMWE fabricated using a tightening torque of 12 N m, and a hot-pressing pressure of 6 MPa. These conditions result in the best performance and lowest overvoltages obtained for this system to date. No significant concentration overvoltage is observed even at 5 A cm^{-2} in the high current density region, confirming that this unique GDE is highly suited for PEMWE operation at high current densities. Water electrolysis voltage of 1.7 V at 1 A cm^{-2} (1.7 W cm^{-2}) and 2.5 V at 5 A cm^{-2} (12.5 W cm^{-2}) with the iridium loading of 0.172 $mg_{\text{-Ir}}$ cm^{-2} corresponds to an iridium loading per electric power of 0.1 $mg_{\text{-Ir}}$ W^{-1} and 0.014 $mg_{\text{-Ir}}$ W^{-1}, respectively. These values are more than one order of magnitude lower than the target of 2.7 $mg_{\text{-Ir}}$ W^{-1}

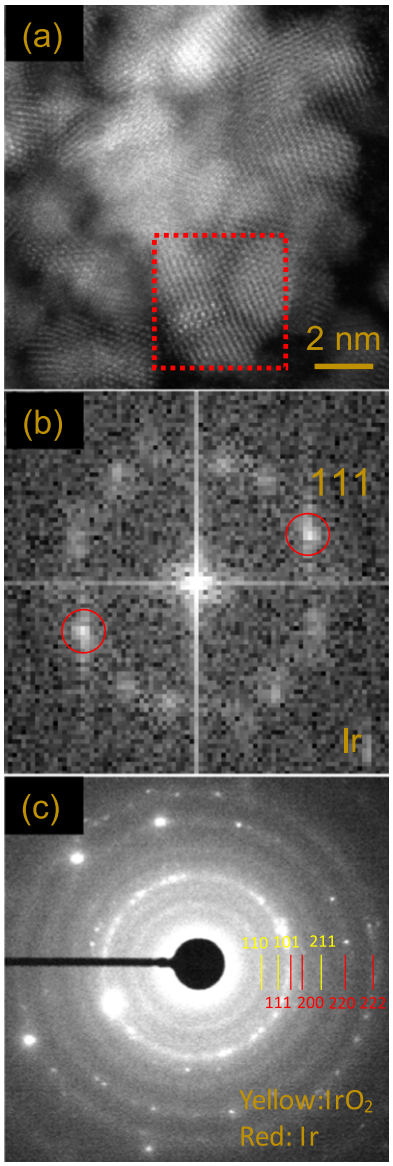

Figure 19. (a) Higher-magnification STEM image of iridium nanoparticles deposited onto titanium GDEs by APD (4,000 pulses), after potential cycling using the durability Protocol (II). (b) Fast Fourier transform (FFT) of the region highlighted in red in (a). The FCC crystal structure corresponds to that of metallic iridium. (c) SAED pattern taken from Fig. 18a.

by 2020, and the target of 0.4 $mg_{\text{-Ir}}$ W^{-1} by 2030 has also been achieved, as described in the Introduction.[24] These facts confirm the technological relevance of these unique catalyst-integrated GDEs for PEMWEs.

Conclusions

Catalyst-integrated gas diffusion electrodes (GDEs) were developed for polymer electrolyte membrane water electrolysis (PEMWE) cells. These comprised porous titanium metal supports (acting as gas diffusion layers/current collectors) with nanostructured titanium oxide surfaces (acting as the catalyst support), decorated with iridium metal nanoparticles (acting as the electrocatalyst). The specific surface area of the nanostructured titanium oxide surface was improved by optimizing the NaOH etching conditions. The Ir loading was optimized by varying the number of arc plasma deposition (APD) pulses. These GDEs exhibited comparable performance for water electrolysis to commercial

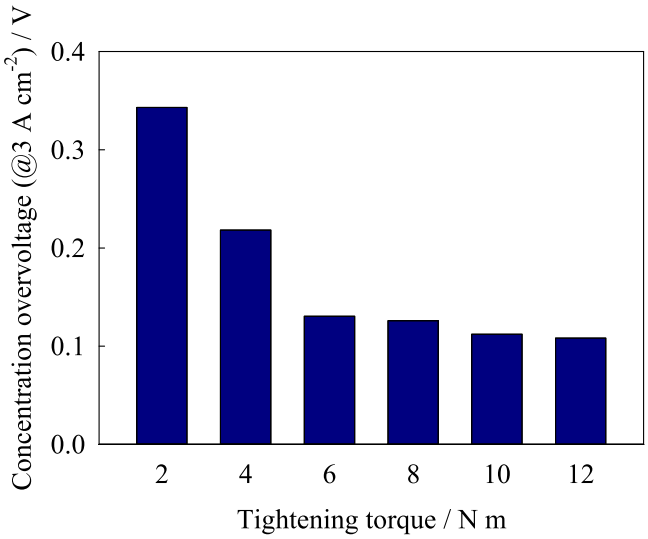

Figure 20. Variation of the concentration overvoltage measured at 3 A cm^{-2}, for catalyst-integrated GDEs prepared using different tightening torques. The hot-pressing pressure was fixed at 3 MPa.

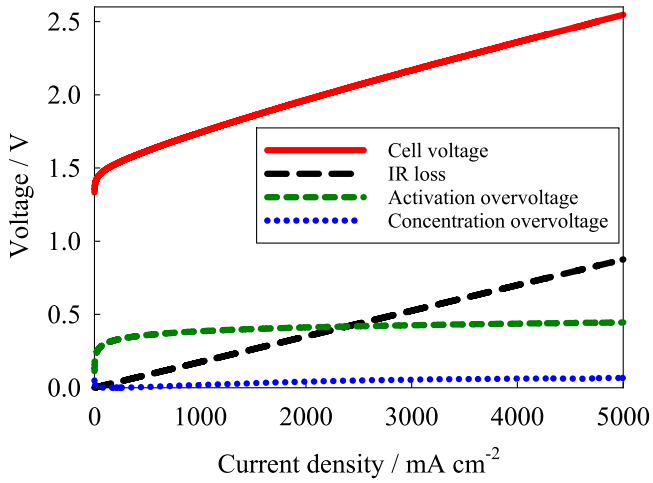

Figure 21. I–V characteristics and overvoltages, at 80 °C, of a PEMWE cell using an optimized catalyst-integrated GDE, prepared using a tightening torque of 12 N m, and hot-press pressure of 6 MPa. The iridium loading was 0.172 $mg_{\text{-Ir}}$ cm^{-2} at the anode.

iridium-based catalysts. The durability was reasonable, but requires further improvement to compete with commercial electrocatalysts. Meanwhile, suitable performance was obtained at high current density up to 5 A cm^{-2} in a fully optimized PEMWE cell. This unique GDE structure is an important proof-of-concept for simplified PEMWEs with decreased thickness, fewer components, and lower iridium loading, and will eventually translate to lower cost systems. The catalyst-integrated GDE concept presented could be described as having a titanium/titanium oxide pseudo "core–shell microstructure", while the outermost surface of the metallic Ir catalyst nanoparticles is oxidized, forming an iridium/iridium oxide "core–shell nanostructure".

Acknowledgments

Financial support from the Center of Innovation (COI) Program Grant Number JPMJCE1318 by the Japan Science and Technology Agency (JST) is gratefully acknowledged. A partial financial support by the Fukuoka Strategy Conference for Hydrogen Energy is also acknowledged.

ORCID

Akari Hayashi https://orcid.org/0000-0003-1753-2241
Kazunari Sasaki https://orcid.org/0000-0002-3174-9087

References

1. Hydrogen Council, Hydrogen Scaling up, November 2017. [https://hydrogencouncil.com/wp-content/uploads/2017/11/Hydrogen-scaling-up-Hydrogen-Council.pdf] (accessed 2020. 5. 21).
2. International Energy Agency, The Future of Hydrogen, 2019. [https://iea.org/hydrogen2019/] (accessed 2020. 5. 21).
3. D. O. Akinyele and R. K. Rayudu, *Sustainable Energy Technologies and Assessments*, **8**, 74 (2014).
4. M. A. Pellow, C. J. M. Emmott, C. J. Barnhart, and S. M. Benson, *Energy Environ. Sci.*, **8**, 1938 (2015).
5. Q. Feng, X. Z. Yuan, G. Liu, B. Wei, Z. Zhang, H. Li, and H. Wang, *J. Power Sources*, **366**, 33 (2017).
6. K. Mazloomi and C. Gomes, *Renew. Sustain. Energy Rev.*, **16**, 3024 (2012).
7. M. Momirlan and T. N. Veziroglu, *Int. J. Hydrogen Energy*, **30**, 759 (2005).
8. K. T. Møller, T. R. Jensen, E. Akiba, and H. Li, *Progress in Natural Science: Materials International*, **27**, 34 (2017).
9. M. B. Ley et al., *Mater. Today*, **17**, 122 (2014).
10. S. S. Kumar and V. Himabindu, *Materials Science for Energy Technologies*, **2**, 442 (2019).
11. S. A. Grigoriev, V. I. Porembsky, and V. N. Fateev, *Int. J. Hydrogen Energy*, **31**, 171 (2006).
12. M. Carmo, D. L. Fritz, J. Mergel, and D. Stolen, *Int. J. Hydrogen Energy*, **38**, 4901 (2013).
13. P. Millet, *Compedium of Hydrogen Energy*, ed. V. Subramani et al. (Woodhead Publishing, Elsevier, Cambridge, United Kingdom) p. 255 (2015).
14. D. Bessarabov, H. Wang, H. Li, and N. Zhao, *PEM Electrolysis for Hydrogen Production* (CRC Press, Boca Raton, FL) (2016).
15. M. M. Rashid, M. K. A. Mesfer, H. Naseem, and M. Danish, *Int. J. Eng. Adv. Technol.*, **4**, 80 (2015).
16. B. Bladergroen, H. Su, S. Pasupathi, and V. Linkov, *Electrolysis*, ed. J. Kleperis and V. Linkov (InTech, Rijeka, Croatia) p. 45 (2012).
17. C. Rakousky, U. Reimer, K. Wippermann, S. Kuhri, M. Carmo, W. Lueke, and D. Stolten, *J. Power Sources*, **342**, 38 (2017).
18. A. S. Aricò, S. Siracusano, N. Briguglio, A. D. Blasi, and V. Antonucci, *J. Appl. Electrochem.*, **43**, 107 (2012).
19. U. Babic, M. Suermann, F. N. Büchi, L. Gubler, and T. J. Schmidt, *J. Electrochem. Soc.*, **164**, F387 (2017).
20. K. Ito, T. Sakaguchi, and Y. Tsuchiya, *Hydrogen Energy Engineering: A Japanese Perspective*, ed. K. Sasaki et al. (Springer, Japan) p. 143 (2016).
21. P. Donohoo-Vallett et al., U.S. Department of Energy. "Revolution…Now: The Future Arrives for Five Clean Energy Technologies −2016 Update". September 2016. [https://energy.gov/sites/prod/files/2016/09/f33/Revolutiona%CC%82%E2%82%ACNow%202016%20Report_2.pdf] (accessed 21st May 2020).
22. B. Pivovar, N. Rustagi, and S. Satyapal, *The Electrochemical Society Interface*, **27**, 47 (2018).
23. C. Rakousky, U. Reimer, K. Wippermann, M. Carmo, W. Lueke, and D. Stolen, *J. Power Sources*, **326**, 120 (2016).
24. Hydrogen and Fuel cell strategy Council, Ministry of Economy, Trade and Industry, Japanese government, September 11, 2019 (in Japanese). [https://meti.go.jp/shingikai/energy_environment/suiso_nenryo/pdf/017_03_01.pdf] (accessed 21st May 2020).
25. F. Godínez-Salomón, L. Albiter, S. M. Alia, B. S. Pivovar, L. E. Camacho-Forero, P. B. Balbuena, R. Mendoza-Cruz, M. J. Arellano-Jimenez, and C. P. Rhodes, *ACS Catal.*, **8**, 10498 (2018).
26. S. M. Alia, S. Shulda, C. Ngo, S. Pylypenko, and B. S. Pivovar, *ACS Catal.*, **8**, 2111 (2018).
27. H. N. Nong, L. Gan, E. Willinger, D. Teschner, and P. Strasser, *Chem. Sci.*, **5**, 2955 (2014).
28. T. Reier, Z. Pawolek, S. Cherevko, M. Bruns, T. Jones, D. Teschner, S. R. Selve, A. Bergmann, H. N. Nong, and R. Schlögl, *J. Am. Chem. Soc.*, **137**, 13031 (2015).
29. J. Cheng, H. Zhang, G. Chen, and Y. Zhang, *Electrochim. Acta*, **54**, 6250 (2009).
30. K. C. Neyerlin, G. Bugosh, R. Forgie, Z. Liu, and P. Strasser, *J. Electrochem. Soc.*, **156**, 363 (2009).
31. Z.-X. Lu, Y. Shi, C.-F. Yan, C.-Q. Guo, and Z.-D. Wang, *Int. J. Hydrogen Energy*, **42**, 3572 (2017).
32. G. Y. Chen, S. R. Bare, and T. E. Mallouk, *J. Electrochem. Soc.*, **149**, A1092 (2002).
33. S. Siracusano, V. Baglio, C. D'Urso, V. Antonucci, and A. S. Aricò, *Electrochim. Acta*, **54**, 6292 (2009).
34. Y. Murakami, H. Ohkawauchi, M. Ito, K. Yahikozawa, and Y. Takasu, *Electrochim. Acta*, **39**, 2551 (1994).
35. A. Marshall, B. Børresen, G. Hagen, M. Tsypkin, and R. Tunold, *Energy*, **32**, 431 (2007).
36. A. T. Marshall, S. Sunde, M. Tsypkin, and R. Tunold, *Int. J. Hydrogen Energy*, **32**, 2320 (2007).
37. H. Anai, J. Matusda, Z. Noda, Y. Tachikawa, A. Hayashi, K. Ito, and K. Sasaki, *ECS Trans.*, **75**, 1129 (2016).
38. Y. Murakami, S. Tsuchiya, K. Yahikozawa, and Y. Takasu, *Electrochim. Acta*, **39**, 651 (1994).
39. A. J. Terezo, J. Bisquert, E. C. Pereira, and G. Garcia-Belmonte, *J. Electroanal. Chem.*, **508**, 59 (2001).
40. V. K. Puthiyapura, S. Pasupathi, H. Su, X. Liu, B. Pollet, and K. Scott, *Int. J. Hydrogen Energy*, **39**, 1905 (2014).
41. J. Polonský, P. Mazúr, M. Paidar, E. Christensen, and K. Bouzek, *Int. J. Hydrogen Energy*, **39**, 3072 (2014).
42. L. Ma, S. Sui, and Y. Zhai, *Int. J. Hydrogen Energy*, **34**, 678 (2009).
43. A. V. Nikiforov, A. L. Tomás García, I. M. Petrushina, E. Christensen, and N. J. Bjerrum, *Int. J. Hydrogen Energy*, **36**, 5797 (2011).
44. T. Ioroi, Z. Siroma, N. Fujiwara, S. Yamazaki, and K. Yasuda, *Electrochem. Comm.*, **7**, 183 (2005).
45. K. Kakinuma, M. Uchida, T. Kamino, H. Uchida, and M. Watanabe, *Electrochim. Acta*, **56**, 2881 (2011).
46. K. Sasaki, F. Takasaki, Z. Noda, S. Hayashi, Y. Shiratori, and K. Ito, *ECS Trans.*, **33**, 473 (2010).
47. S. Matsumoto, M. Nagamine, Z. Noda, J. Matsuda, S. M. Lyth, A. Hayashi, and K. Sasaki, *J. Electrochem. Soc.*, **165**, 1165 (2018).
48. M. Iwami, D. Horiguchi, Z. Noda, A. Hayashi, and K. Sasaki, *ECS Trans.*, **69**, 603 (2015).
49. Y. Nakazato, D. Kawachino, Z. Noda, J. Matsuda, S. M. Lyth, A. Hayashi, and K. Sasaki, *J. Electrochem. Soc.*, **165**, 1154 (2018).
50. D. Kawachino, Z. Noda, J. Matsuda, A. Hayashi, and K. Sasaki, *ECS Trans.*, **80**, 781 (2017).
51. D. Kawachino, M. Yasutake, H. Odoi, Z. Noda, J. Matsuda, A. Hayashi, and K. Sasaki, *ECS Trans.*, **86**, 541 (2018).
52. M. Yasutake, H. Anai, D. Kawachino, Z. Noda, J. Matsuda, K. Ito, A. Hayashi, and K. Sasaki, *ECS Trans.*, **86**, 673 (2018).
53. M. Yasutake, D. Kawachino, Z. Noda, J. Matsuda, K. Ito, A. Hayashi, and K. Sasaki, *ECS Trans.*, **92**, 833 (2019).
54. H. Odoi, Z. Noda, J. Matsuda, A. Hayashi, and K. Sasaki, *ECS Trans.*, **86**, 461 (2018).
55. H. Odoi, D. Kawachino, Z. Noda, J. Matsuda, A. Hayashi, and K. Sasaki, *ECS Trans.*, **92**, 507 (2019).
56. J. V. Muylder and M. Pourbaix, *Atlas of Electrochemical Equilibria on Aqueous Solutions*, ed. M. Pourbaix and J. A. Franklin (National Association of Corrosion Engineers, Houston, TX) p. 373 (1974).
57. H. B. Beer, *J. Electrochem. Soc.*, **127**, 303C (1980).
58. M. S. Wilson and S. Gottesfeld, *J. Appl. Electrochem.*, **22**, 1 (1992).
59. S. C. Singhal and K. Kendall, *High Temperature Solid Oxide Fuel Cells* (Elsevier, Amsterdam) (2003).
60. R. G. Allen, C. Lim, L. X. Yang, K. Scott, and S. Roy, *J. Power Sources*, **143**, 142 (2005).
61. T. Ioroi, K. Yasuda, Z. Siroma, N. Fujiwara, and Y. Miyazaki, *J. Power Sources*, **112**, 583 (2002).
62. Y. Agawa, M. Kunimatsu, T. Ito, and Y. Kuwahara, *ECS Electrochem. Lett.*, **4**, 57 (2015).
63. S. M. Alia, B. Rasimick, C. Ngo, K. C. Neyerlin, S. S. Kocha, S. Pylypenko, H. Xu, and B. S. Pivovar, *J. Electrochem. Soc.*, **163**, 3105 (2016).
64. S. M. Alia and G. C. Anderson, *J. Electrochem. Soc.*, **166**, 282 (2019).
65. M. Okumura, Z. Noda, J. Matsuda, Y. Tachikawa, M. Nishihara, S. M. Lyth, A. Hayashi, and K. Sasaki, *J. Electrochem. Soc.*, **164**, F928 (2017).
66. M. Muto, M. Nagayama, K. Sasaki, and A. Hayashi, *ECS Trans.*, **86**, 719 (2018).
67. Y. Q. Wang, G. Q. Hu, X. F. Duan, H. L. Sun, and Q. K. Xue, *Chem. Phys. Lett.*, **365**, 427 (2002).
68. Y. F. Chen, C. Y. Lee, M. Y. Yeng, and H. T. Chiu, *Mater. Chem. Phys.*, **80**, 39 (2003).
69. Q. Chen, G. H. Du, S. Zhang, and L. M. Peng, *Acta Cryst.*, **B58**, 587 (2002).
70. D. Kawachino, M. Yasutake, Z. Noda, J. Matsuda, S. M. Lyth, A. Hayashi, and K. Sasaki, *J. Electrochem. Soc.*, **167**, 104513 (2020).
71. T. A. Zawodzinski Jr, M. Neeman, L. O. Sillerud, and S. Gottesfeld, *J. Phys. Chem.*, **95**, 6040 (1991).
72. J. Mališ, P. Mazúr, M. Paidar, T. Bystron, and K. Bouzek, *Int. J. Hydrogen Energy*, **41**, 2177 (2016).
73. M. Carmo, D. L. Fritz, J. Mergel, and D. Stolten, *Intl. J. Hydrogen Energy*, **38**, 4901 (2013).
74. P. Lettenmeier, S. Kolb, N. Sata, A. Fallisch, L. Zielke, S. Thiele, A. S. Gago, and K. A. Friendrich, *Energy Env. Sci.*, **10**, 2521 (2017).
75. T. Schuler, R. D. Bruycker, T. J. Schmidt, and F. N. Büchi, *J. Electrochem. Soc.*, **166**, 270 (2019).
76. S. Zhao, A. Stocks, B. Rasimick, K. More, and H. Xu, *J. Electrochem. Soc.*, **165**, F82 (2018).
77. C. Rozain, E. Mayousse, N. Guillet, and P. Millet, *Appl. Catalysis B*, **182**, 153 (2016).
78. S. Moravcová, Z. Cílová, and K. Bouzek, *J. Appl. Electrochem.*, **35**, 991 (2005).
79. S. Cherevko, S. Geiger, O. Kasian, A. Mingers, and K. J. J. Mayhofer, *J. Electroanalytical Chem.*, **773**, 69 (2016).
80. S. Cherevko, S. Geiger, O. Kasian, A. Mingers, and K. J. J. Mayhofer, *J. Electroanalytical Chem.*, **774**, 102 (2016).
81. S. A. Shakhshir, X. Cui, S. Frensch, and S. K. Kær, *Int. J. Hydrogen Energy*, **42**, 21597 (2017).
82. E. Borgardt, L. Giesenberg, M. Reska, M. Müller, K. Wippermann, M. Langemann, W. Lehnert, and D. Stolten, *Int. J. Hydrogen Energy*, **44**, 23556 (2019).
83. S. H. Frensch, A. C. Olesen, S. S. Araya, and S. K. Kær, *Electrochim. Acta*, **263**, 228 (2018).
84. O. F. Selamet and M. S. Ergoktas, *J. Power Sources*, **281**, 103 (2015).